Measurement and assignment of double-resonance transitions to the 8900-9100-cm(-1) levels of methane

Aleksandra Foltynowicz, Lucile Rutkowski, Isak Silander, Alexandra C. Johansson, Vinicius Silva de Oliveira, Ove Axner, Grzegorz Sobon, Tadeusz Martynkien, Pawel Mergo, Kevin K. Lehmann

Measurement and assignment of double-resonance transitions to the 8900–9100-cm^{-1} levels of methane

Aleksandra Foltynowicz,[1,*] Lucile Rutkowski,[2] Isak Silander,[1] Alexandra C. Johansson,[1] Vinicius Silva de Oliveira,[1] Ove Axner,[1] Grzegorz Soboń,[3] Tadeusz Martynkien,[4] Paweł Mergo,[5] and Kevin K. Lehmann[6,†]

[1]*Department of Physics, Umeå University, 901 87 Umeå, Sweden*

[2]*Université de Rennes, CNRS, IPR (Institut de Physique de Rennes), UMR 6251, F-35000 Rennes, France*

[3]*Laser & Fiber Electronics Group, Faculty of Electronics, Wrocław University of Science and Technology, 50-370 Wroclaw, Poland*

[4]*Faculty of Fundamental Problems of Technology, Wrocław University of Science and Technology, 50-370 Wroclaw, Poland*

[5]*Laboratory of Optical Fiber Technology, Maria Curie-Sklodowska University, 20-031 Lublin, Poland*

[6]*Departments of Chemistry & Physics, University of Virginia, Charlottesville, Virginia 22904, USA*

(Received 8 July 2020; revised 16 October 2020; accepted 1 December 2020; published 11 February 2021)

Optical-optical double-resonance spectroscopy with a continuous wave pump and frequency comb probe allows measurement of sub-Doppler transitions to highly excited molecular states over a wide spectral range with high frequency accuracy. We report on assessment and characterization of sub-Doppler double-resonance transitions in methane measured using a 3.3-μm continuous wave optical parametric oscillator as a pump and a 1.67-μm frequency comb as a probe. The comb spectra were recorded using a Fourier transform spectrometer with comb-mode-limited resolution. With the pump tuned to nine different transitions in the ν_3 fundamental band, we detected 36 ladder-type transitions to the $3\nu_3$ overtone band region, and 18 V-type transitions to the $2\nu_3$ overtone band. We describe in detail the experimental approach and the pump stabilization scheme, which currently limits the frequency accuracy of the measurement. We present the data analysis procedure used to extract the frequencies and intensities of the probe transitions for parallel and perpendicular relative pump-probe polarization. We compare the center frequencies and relative intensities of the ladder-type transitions to theoretical predictions from the TheoReTS and ExoMol line lists, demonstrating good agreement with TheoReTS.

DOI: 10.1103/PhysRevA.103.022810

I. INTRODUCTION

Methane has long been a molecule of intense scientific interest [1,2]. It is an increasingly important fossil fuel and greenhouse contributor [3], and it is produced or consumed by many anaerobic organisms [4]. It is also the dominant source of the opacity of many of the planets in our solar system [5] and has been detected in the atmospheres of hot-Jupiter exoplanets [6–8]. Accurate modeling of high-temperature spectra of methane is important for astrophysical [9] and combustion [10] applications. Currently, the most accurate and extensive high-temperature methane line list is based on the combination of *ab initio* calculations from the TheoReTS database [11] and the HITRAN2016 data [12]. However, the lack of experimental high-temperature spectra prevents validation of the accuracy of the theoretical predictions at temperatures above 1000 K [12,13]. Heating the sample to reach these temperatures under controlled conditions is an experimental challenge, because methane decomposes to graphite and hydrogen on warm surfaces, and the gas-phase spectra are congested and difficult to assign [13–15].

The dominant spectroscopic signature of methane is its vibration-rotation spectrum, including weak overtone and combination bands extending into the visible spectral region. Because of the near-coincidence of the normal mode frequencies ($\nu_1 \sim \nu_3 \sim 2\nu_2 \sim 2\nu_4$) and strong couplings between them caused by the Fermi, Darling-Dennison, and Coriolis resonances, the energy levels of methane form clumps of strongly interacting states known as polyads [16]. The complexity of methane spectra and their analysis rises rapidly with increasing excitation energy and with temperature. The ν_3 fundamental C-H stretch band at 3000 cm^{-1} has been well characterized. The pioneering saturation spectroscopy studies investigated the temperature and pressure shift of the $P(7)$ line at 3.39 μm [17,18]. More recently high-accuracy experimental line lists were obtained using frequency comb-referenced saturation spectroscopy [19–21]. The $2\nu_3$ first overtone band at 6000 cm^{-1} has also been investigated thoroughly. Absolute transition frequencies were determined using saturation spectroscopy [22,23] and Doppler-broadened dual comb spectroscopy [24], and extensive room- and low-temperature line lists including broadening parameters have been reported

*aleksandra.foltynowicz@umu.se
†kl6c@virginia.edu

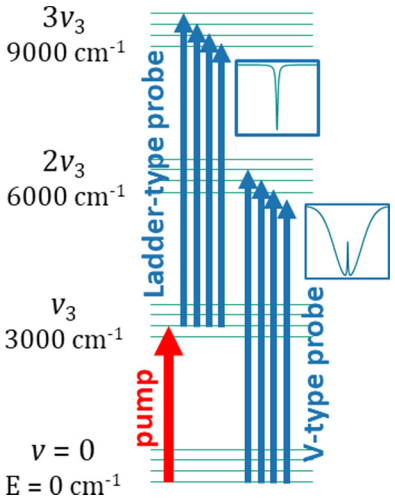

FIG. 1. Energy level structure of the ν_3 C-H stretching bands of methane with the pump transition indicated in red and comb probe transitions indicated in blue.

based on Fourier transform infrared (FTIR) spectroscopy [25–28] and cavity ring-down spectroscopy [29–31]. Recently, Ghysels *et al.* used a diode laser spectrometer to record spectra at 1000 K in the Tetradecad region (5693–6257 cm^{-1}, dominated by the $2\nu_3$ band) [14] and Wong *et al.* recorded FTIR spectra in the 5400–9000-cm^{-1} range (up to the Triacontad range) at temperatures up to 1000 K [13]. In both cases, the high-temperature spectra were compared to predictions from the TheoReTS line list and very good agreement was found up to the Icosad polyad (7700 cm^{-1}). The agreement in the 8200–8900-cm^{-1} range, part of the Triacontad range, was worse, limited by the inaccuracies in the line lists caused by the lack of experimentally assigned spectra, which prevents empirical corrections to line positions. Recently, Nikitin *et al.* presented an improved low- and room-temperature line list in the 8850–9180-cm^{-1} range based on FTIR measurements [32], again finding good agreement with the TheoReTS predictions from the ground state. However, firmly assigned transitions to the $3\nu_3$ overtone band region starting from highly excited levels are still largely missing from the literature. De Martino *et al.* used optical-optical double-resonance spectroscopy with 1.6-μm pump and 3.3-μm probe nanosecond pulses to measure transitions from the $2\nu_3$ to the $3\nu_3$ band [33–35]. The resolution of this pioneering work was limited by the optical sources to $>0.12\,\text{cm}^{-1}$, and the frequency accuracy was estimated to be $0.03\,\text{cm}^{-1}$. Thus both the resolution and accuracy were substantially worse than the Doppler width of methane transitions ($\sim 0.01\,\text{cm}^{-1}$ full width at 3.3 μm and 300 K).

In Companion Paper [36], we demonstrated the implementation of optical-optical sub-Doppler resolution molecular double-resonance spectroscopy using a continuous wave (cw) pump and a frequency comb probe and measured transitions from the ν_3 fundamental band of methane to the $3\nu_3$ overtone band region, as shown schematically in Fig. 1. The wide spectral coverage and high frequency accuracy of the comb probe allowed detection of a larger number of transitions with orders of magnitude better frequency accuracy than previous double-resonance measurements [33–35]. The saturating cw pump laser addresses assigned transitions in the ν_3 fundamental C-H stretching band and transfers population from the lower quantum state to the upper. The comb is used to simultaneously probe transitions from the upper level of the pump transition to levels in the $3\nu_3$ region (ladder-type transitions), and from the depleted rotational state of the ground vibrational state to the $2\nu_3$ levels (the V-type transitions). Since the pump is monochromatic (linewidth <1 MHz), only a narrow velocity group of molecules is excited by it, and the resulting probe transitions are Doppler free, with a width limited by the homogeneous broadening [37]. This marks the double-resonance transitions among the Doppler-broadened transitions of the $2\nu_3$ band. The V-type probe transitions appear as narrow dips in the Doppler-broadened lines sharing the lower level with the pump transition, while the ladder-type probe transitions appear as sub-Doppler absorption lines (see insets in Fig. 1). The ratio of the probe transition intensities measured with different relative polarizations of the two fields depends on the change in rotational quanta of the pump and probe transitions [38] and can be used to assign the quantum number of the upper state.

The ladder-type transitions allow reaching levels that are not allowed from the ground vibrational state. In the case of CH_4, transitions starting in the vibrational ground state are only allowed to vibrational states with F_2 symmetry, but from the F_2 symmetry ν_3 level transitions are allowed to vibrational states with A_1, E, F_1, and F_2 vibrational symmetries (but not A_2). The final states reached in this work are part of the $n = 2\nu_1 + 2\nu_3 + \nu_2 + \nu_4 = 6$ polyad, known as the Triacontad as there are 30 ways to distribute the vibrational quanta consistent with $n = 6$ [16]. However, this understates the expected complexity as most of these states have multiple quanta in degenerate vibrational modes and this leads to 280 distinct vibrational states (41 A_1, 20 A_2, 58 E, 71 F_1, and 90 F_2 symmetries) [16]. Coriolis interactions lift the degeneracy of the E, F_1, and F_2 vibrational states leading to a total of 660 unique vibrational states.

In this paper, we describe in detail the experimental implementation of optical-optical double-resonance spectroscopy using a cw pump and a frequency comb probe. We present the pump and probe frequency stabilization schemes, the data acquisition procedures, the method of detection of probe transitions, data processing and analysis, and the fitting routines. We list the frequencies and widths of all detected V-type and ladder-type probe transitions, and the term values of the final states in the 8900–9100-cm^{-1} range reached by the ladder-type excitation. We compare these term values to those reached in the previous double-resonance measurements [33–35]. We compare the frequencies and intensities of the ladder-type probe transitions to theoretical predictions from the TheoReTS [11,39] and Exomol [40,41] databases.

II. EXPERIMENTAL SETUP AND PROCEDURES

The experimental setup, which was the same as used in Companion Paper [36], is shown in Fig. 2(a). The pump was a singly resonant cw optical parametric oscillator (cw-OPO, Aculight, Argos 2400 SF, module C) with idler tunable in the 3.1–3.7-μm range with up to 1 W of power. The probe was an

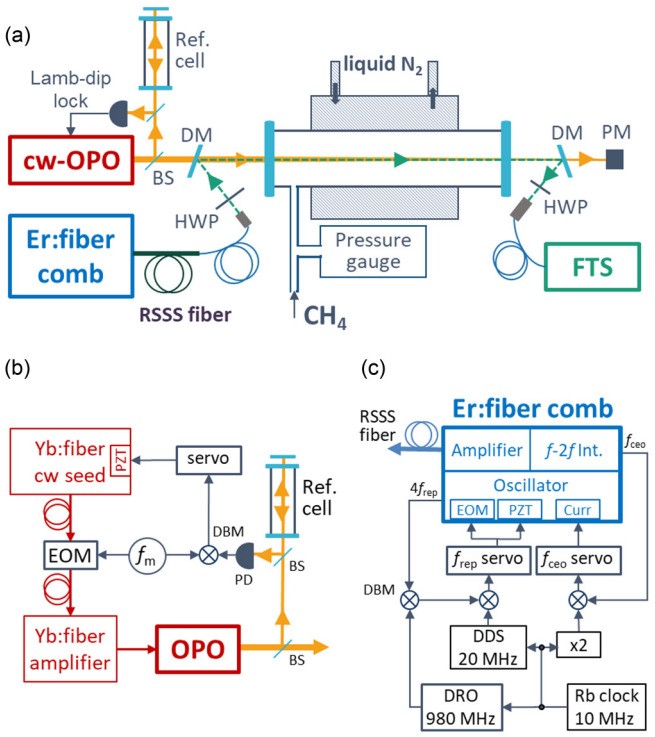

FIG. 2. (a) Experimental setup. cw-OPO: optical parametric oscillator; BS: beam splitter; DM: dichroic mirror; HWP: half-wave plate; RSSS fiber: Raman soliton self-frequency shift microstructured silica fiber; PM: power meter; FTS: Fourier transform spectrometer. (b) Stabilization of the OPO idler frequency. EOM: electro-optic modulator; PZT: piezoelectric transducer; f_m: function generator; DBM: double balanced mixer; PD: photodetector. (c) Stabilization of the frequency comb. Curr: pump diode current; f-$2f$ Int.: f-$2f$ interferometer; DDS: direct digital synthesizer; DRO: dielectric resonator oscillator.

amplified Er:fiber frequency comb (Menlo Systems, FC1500-250-WG) with 250-MHz repetition rate, spectrally shifted to cover a bandwidth of 55 nm (200 cm^{-1}) around 1.67 μm (6000 cm^{-1}). A sample of pure CH_4 (purity 99.995%) was contained in a liquid-nitrogen-cooled single-pass cell with 5-mm-thick uncoated CaF_2 windows. The pump and probe beams were combined using a dichroic mirror in front of the cell and separated using a similar mirror behind the cell. The cw-OPO beam had a Rayleigh range of 1.2 m and the $1/e^2$ intensity radius varied between 1.1 and 1.2 mm along the cooled part of the cell. The comb beam had a waist in the middle of the cell with $1/e^2$ intensity radius of 0.36 mm (a Rayleigh range of 0.25 m). The transmitted probe beam was led via a polarization-maintaining (PM) fiber to a Fourier transform spectrometer (FTS). The polarization of the comb in front of the cell was controlled by the use of a zero-order half-wave plate with design wavelength of 1550 nm and set either parallel or perpendicular to the polarization of the pump. A second half-wave plate was used to align the polarization to the slow axis of the PM fiber.

A. Pump frequency stabilization

The frequency of the idler wave of the cw-OPO was stabilized to the center of a Lamb dip in a selected pump transition

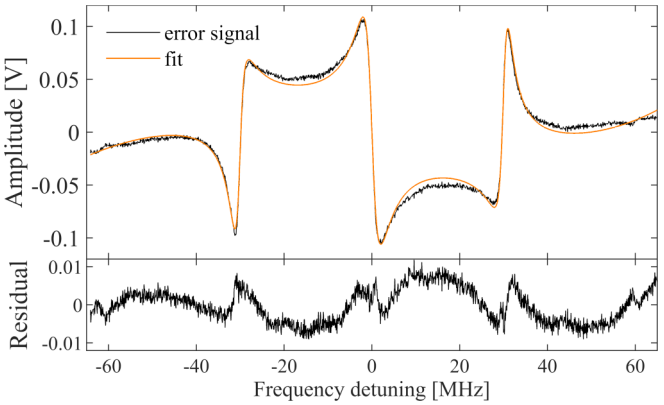

FIG. 3. Frequency modulated Lamb dip error signal (top panel, black) with fit [orange (gray)] and residuum (lower panel).

in the ν_3 fundamental band of CH_4 using a frequency modulated (FM) signal as a frequency discriminator, as shown in Fig. 2(b). The idler frequency was first tuned to the vicinity of the transition using a wavemeter (Burleigh, WA-1500-NIR-89, ± 0.0001 nm resolution, $\pm 2\times 10^{-7}$ absolute relative accuracy) that monitored the pump and signal frequencies (not shown). Part of the beam (50 mW) was directed to a 16.5-cm-long reference cell filled with a few tens of mTorr (a few Pa) of pure methane at room temperature. The idler beam was back reflected, overlapped with the incoming beam, and directed on a high-bandwidth HgCdTd photodiode (PD, VIGO systems, PVI-4TE-8-1x1) using a pellicle beamsplitter. The phase of the idler was modulated at a frequency (f_m) of ~60 MHz (Anritsu MG3692A) with a modulation index of 0.3 via phase modulation of the cw Yb:fiber pump laser using a fiber-coupled electro-optic modulator (EOM, Photline, NIR-MPX-LN-05) inserted between the seed (NKT Photonics, Koheras Adjustik Y-10) and the amplifier (IPG Photonics, YAR-10), as was previously done in Ref. [42]. The detector signal was synchronously demodulated at f_m (using a mixer, amplifier and filters from MiniCircuits) to yield an FM error signal, whose example is shown in Fig. 3. The detection phase was adjusted by fine-tuning the modulation frequency f_m to yield the flattest possible baseline (see below). The error signal was fed to a proportional-integral controller (Newport, LB1005) and the correction was applied to a piezoelectric transducer (PZT) that controls the cavity length of the Yb:fiber seed laser. The closed loop bandwidth was a few kHz.

The FM Lamb dip error signal has contributions from both the Doppler-broadened and sub-Doppler molecular responses, similar to what is observed in cavity-enhanced FM spectroscopy [43]. The shape and amplitude of the two contributions depend strongly on the detection phase and the ratio of the modulation frequency to the linewidths [44,45]. The half width at half maximum (HWHM) of the Doppler-broadened lines in the ν_3 fundamental band at room temperature is 140 MHz, while the HWHM of the Lamb dips is of the order of 1–2 MHz. Thus, for a modulation frequency of 60 MHz the FM signal from the Lamb dip gives rise to three separate features, while that from the Doppler-broadened response constitutes a broad, continuous structure. This implies that the sub-Doppler signals reside on top of a sloping background.

We adjusted the detection phase to make the slope of the Doppler-broadened contribution as flat as possible, while keeping the central feature of the FM Lamb dip signal large.

The sub-Doppler part of the FM error signal as a function of frequency detuning from the center of the transition, $\Delta\nu$, is given by [43]

$$\begin{aligned} &S(\Delta\nu, f_{\mathrm{m}}, \phi, \delta\nu, b) \\ &= S_0\{[\chi^{\mathrm{disp}}(\Delta\nu - f_{\mathrm{m}}/2, b\delta\nu) - 2\chi^{\mathrm{disp}}(\Delta\nu, \delta\nu) \\ &\quad + \chi^{\mathrm{disp}}(\Delta\nu + f_{\mathrm{m}}/2, b\delta\nu)]\cos\phi \\ &\quad + [\chi^{\mathrm{abs}}(\Delta\nu - f_{\mathrm{m}}/2, b\delta\nu) - \chi^{\mathrm{abs}}(\Delta\nu + f_{\mathrm{m}}/2, b\delta\nu)]\sin\phi\}, \end{aligned} \tag{1}$$

where $\chi^{\mathrm{abs}}(\Delta\nu, \delta\nu)$ is the area-normalized Lorentzian absorption function with HWHM of $\delta\nu$, $\chi^{\mathrm{disp}}(\Delta\nu, \delta\nu)$ is its dispersion counterpart, S_0 is an amplitude factor, which is a function of the laser power, modulation index, molecular absorption, and electronic gain, and ϕ is the detection phase. The error signal consists of three features, one at the center of the transition, and two side features separated from the central one by half of the modulation frequency, $\pm f_{\mathrm{m}}/2$ (see Fig. 7.6 in Ref. [46]). The central sub-Doppler feature comprises only a dispersionlike signal that originates mostly from a carrier-carrier interaction, i.e., the Bennett hole burned by the carrier field and detected by the counterpropagating carrier. At a detuning equal to half the modulation frequency, i.e., at $\pm f_{\mathrm{m}}/2$, the sub-Doppler features are a combination of absorption and dispersion signals (at arbitrary detection phase), originating from the carrier-sideband interactions, i.e., the Bennett hole burned by the carrier and detected by the counterpropagating FM sideband and a Bennett hole burned by the sideband and detected by the carrier. This implies that the degrees of saturation are dissimilar for the center and side sub-Doppler features. Since this leads to different power broadening, the widths of the central and side features are different. To reflect this, the width of the side features is multiplied by a scaling factor b (<1) in Eq. (1).

The upper panel of Fig. 3 shows in black the open loop error signal recorded for the ν_3 $R(0)$ line at 70 mTorr with 50 mW of incident power while scanning the Yb:fiber seed laser frequency using the PZT. The orange (gray) curve shows a fit of a sum of Eq. (1) and a second order polynomial (used to model the slowly varying Doppler-broadened background). The PZT voltage was converted to a frequency scale using a linear interpolation between the zero crossings of the three sub-Doppler features (which are separated by $f_{\mathrm{m}}/2$). The fitting parameters were S_0, $\delta\nu$, b, and ϕ, and the fit returned $\delta\nu = 2.06(1)$ MHz, $b = 0.67(1)$, and $\phi = 0.42(2)$ rad. The sharp features in the residuum (lower panel) at detunings of –30, 0, and 30 MHz originate from inaccuracies in the frequency scale calibration (caused by nonlinearities in the PZT response), while the slowly varying structure originates from the remaining Doppler-broadened background, etalon signals, and residual amplitude modulation (RAM).

The error signal drifted over time because of RAM in the cw-OPO output, originating mostly from the Yb:fiber amplifier [47]. The idler unlocked when the offset of the error signal was equal to ±40% of the peak value. This implies that the idler frequency was stable to within $\pm 0.4\delta\nu = \pm 0.8$ MHz. This translates to an uncertainty in the center frequency of the double-resonance probe transitions of ±1.6 MHz (the factor of 2 comes from the ratio of the probe to pump frequencies, which implies that the Doppler shift produced by an error in the Lamb dip lock is twice larger for the probe than for the pump). In our uncertainty analysis we assumed conservatively that the maximum drift of the center frequency of the probe transitions caused by the drift of the pump frequency was 2 MHz, and that the 1σ uncertainty was equal to 2/3 of that, i.e., 1.3 MHz.

B. Comb probe frequency stabilization

The Er:fiber frequency comb was rf-stabilized to a GPS-referenced Rb oscillator (Symmetricom, TSC 4410A) as shown in Fig. 2(c). The carrier envelope offset frequency, f_{ceo}, was measured using an f-$2f$ interferometer and stabilized at 20 MHz (twice the Rb source frequency) by feeding back to the pump diode current of the Er:fiber oscillator. The fourth harmonic of the repetition rate, f_{rep}, was mixed with a stable 980-MHz signal from a dielectric resonator oscillator (DRO), referenced to the Rb oscillator. The resulting beat signal around 20 MHz was phase-locked to a tunable direct digital synthesizer (DDS) that used the Rb oscillator as a clock. Feedback for f_{rep} stabilization was sent to a PZT and EOM inside the oscillator cavity. During acquisition of spectra, the DDS frequency was stepped by 2.78 Hz to shift the comb repetition rate and decrease the sampling point spacing in the final spectrum from 250 MHz (equal to f_{rep}) to 2 MHz (see Sec. II D below).

The output of the Er:fiber oscillator, centered at 1.55 μm, was amplified and fed into a custom-made polarization-maintaining Raman soliton self-frequency shift (RSSS) microstructured silica fiber. The RSSS fiber had a nonlinear coefficient of $9.8\,\mathrm{W^{-1}\,km^{-1}}$ and anomalous dispersion of $\sim 26\,\mathrm{ps\,nm^{-1}\,km^{-1}}$ at 1.56 μm and provided a coherent and efficient wavelength shift [48]. High modal birefringence (at the level of 5×10^{-4}) ensured a high polarization extinction ratio of >20 dB. The center wavelength of the shifted soliton was easily tuned by adjusting the output power of the amplifier, and it was set to 1.67 μm, where the simultaneous coverage was $200\,\mathrm{cm^{-1}}$ with 20 mW of power out of the RSSS fiber.

C. Sample conditions

The sample cell was 80 cm long and the central 55-cm-long part was cooled by liquid nitrogen to increase the absorption signal of the low rotational quantum number states addressed in this work. For transitions starting from states with $J_{\mathrm{low}} = 0$ and 1, the absorption coefficient at fixed pressure is proportional to the number density (which has a T^{-1} dependence, where T is the absolute temperature of the sample), the inverse of the partition function (which yields a $T^{-3/2}$ dependence for the rotational partition function of a nonlinear molecule [49]), and the normalized line shape function (which has a $T^{-1/2}$ dependence for Doppler-broadened transitions). This gives a net T^{-3} dependence, so at a given pressure the peak absorption coefficient of those transitions is expected to be 56 times stronger at $T = 77$ K than at room temperature. At the actual sample temperature of 111 K (see Sec. III A below), the

TABLE I. Experimental conditions for the different pump transitions. Column 1 shows the pump transition, column 2 states the pressure at which the measurement was performed, while the corresponding linear peak absorption coefficient α and the saturation intensity are listed in columns 3 and 4, respectively, where M is the quantum number for the projection of total angular momentum on the axis defined by the pump electric field. Since the pump polarization is by definition parallel to the quantization axis, both states in the pump transition have the same M quantum number. Column 5 displays the pump power measured behind the cell when the pump was unlocked and detuned from the transition (off resonance), and locked to the transition (on resonance), while column 6 gives the calculated on-axis intensity at the input to the cell (corrected for transmission of the CaF_2 window and the dichroic mirror). Column 7 indicates the number of averaged spectra, where $\perp$ and $\parallel$ stand for perpendicular and parallel relative pump-probe polarizations, respectively.

Pump transition	Sample pressure (mTorr)	α at 111 K (cm^{-1})	Saturation intensity at 111 K (mW/mm^2)	Transmitted pump power off, on resonance (mW)	Input pump intensity (mW/mm^2)	No. averages
$R(0)$	30	0.171	1.46 ($M=0$)	850, 150	500	16 $\perp$ 11 $\parallel$
$R(1)$	30	0.151	4.38 ($M=0$) 2.19 ($M=\pm1$)	890, 170	520	16
$Q(1)$	35	0.103	3.53 ($M=\pm1$)	890, 170	520	16
$P(1)$	60	0.058	17.5 ($M=0$)	850, 152 $\perp$ 867, 175 $\parallel$	500 $\perp$ 510 $\parallel$	17 $\perp$ 5 $\parallel$
$P(2,E)$	58	0.085	13.6 ($M=0$) 18.2 ($M=\pm1$)	1130, 208	660	15 $\perp$ 11 $\parallel$
$P(2,F_2)$	40	0.088	6.49 ($M=0$) 8.65 ($M=\pm1$)	940, 194	550	10 $\perp$ 16 $\parallel$
$P(3,A_2)$	33	0.132	4.12 ($M=0$) 4.84 ($M=\pm1$) 12.4 ($M=\pm2$)	850, 126	500	16 $\perp$ 8 $\parallel$
$P(3,F_1)$	33	0.079	4.12 ($M=0$) 4.84 ($M=\pm1$) 12.4 ($M=\pm2$)	850, 156	500	16 $\perp$ 12 $\parallel$
$P(3,F_2)$	33	0.079	4.12 ($M=0$) 4.84 ($M=\pm1$) 12.4 ($M=\pm2$)	700, 140	410	16 $\perp$ 9 $\parallel$

absorption signal for those transitions is enhanced by a factor of 19 compared to room temperature.

The methane pressure in the cell was adjusted so that the transmittance of the pump power on resonance was 20%, which was found to yield a maximum V-type probe signal. The pressure in the cell was monitored using a capacitive vacuum gauge (Leybold, Ceravac CTR 101, max range 1 Torr, 0.12% relative uncertainty). The pump power transmitted through the cell was monitored during the acquisition using a power meter (Thorlabs, S302C). This allowed rejecting the spectra for which the cw-OPO idler unlocked from the pump transition, which manifested itself as an increase of transmitted power.

Table I summarizes the experimental conditions for all measurements with pump locked to nine different transitions in the ν_3 fundamental band, listed in column 1. Column 2 shows the CH_4 pressure in the cell, while columns 3 and 4 display the corresponding linear absorption coefficient on resonance, α, and the saturation intensity for the different M (Zeeman magnetic) sublevels, respectively, both calculated at a temperature of 111 K. The absorption coefficient was calculated assuming a Gaussian line shape function and using the line intensities from the HITRAN database [50]. To calculate the saturation intensities, we used relaxation rates obtained by scaling the room temperature pressure self-broadening coefficients listed in HITRAN [50], assuming a hard-sphere collision model, i.e., $T^{-1/2}$ dependence. Transition dipole moments were calculated from the Einstein A coefficients for the pump transitions listed in the HITRAN database [50], which are close to $25\,s^{-1}$ for all transitions addressed in this work. The transmitted pump power measured off and on resonance (i.e., with pump unlocked and detuned from the transition, or locked to the transition, respectively) is stated in column 5. Column 6 shows the on-axis intensity of the pump beam after the input window of the cell, calculated as the transmitted off-resonance pump power in mW multiplied by $2/(1.15)^2/\pi/T_{CaF2}/T_{DM}$, where $T_{CaF2}=95\%$ is the transmission through the 5-mm-thick uncoated CaF_2 window, $T_{DM}=88\%$ is the transmission through the dichroic mirror, and where a beam radius of 1.15 mm was assumed. The degree of saturation varied between 30 and 340 for the different pump transitions. Column 7 gives the number of spectra averaged; for some spectra the number of averages was different for parallel, $\parallel$, and perpendicular, $\perp$, relative pump-probe polarizations, since the spectra for which the cw-OPO unlocked from the Lamb dip were removed.

D. Spectral acquisition and baseline removal

The comb spectra were measured using a home-built fast-scanning Fourier transform spectrometer (FTS) with autobalanced detection [51] and comb-mode-limited (subnominal) resolution [52,53]. The optical path difference was calibrated using a frequency-stabilized 633-nm HeNe laser (Sios, SL/02/1). The HeNe laser and comb interferograms

were recorded using a digital oscilloscope (National Instruments, PCI-5922, 5 MS/s sampling rate and 20 bit resolution) and the comb interferogram was resampled at the zero crossings and extrema of the HeNe interferogram. To sample the comb modes precisely without the influence of the instrumental line shape, the nominal resolution of the FTS was set equal to the comb f_{rep} (i.e., to 250 MHz) [52,53]. One interferogram was acquired in 5.8 s and yielded a sample point spacing of 250 MHz. The f_{rep} was then tuned 125 times in steps of 2.78 Hz, which resulted in a ~2 MHz shift of the comb modes per step. Spectra taken with the same f_{rep} value were averaged up to 16 times (see Table I). Next, the baseline, originating from the spectral envelope of the laser and etalon signals from multiple reflections in the uncoated cell windows, was removed using cepstral analysis based on the procedure described in Ref. [54]. This method relies on analyzing the spectrum in the time rather than the frequency domain, where the contributions of the baseline and the molecular signal are easier to separate. In particular, the contribution of a slowly varying baseline is present mostly at the shorter times close to the center burst, while the free induction decay of the molecular signal extends to longer times. The baseline correction was done on a 300-cm^{-1}-wide piece of spectrum centered at 6000 cm^{-1} containing 36 000 points spaced by 250 MHz. First, the Doppler-broadened transmission spectrum of the $2\nu_3$ band of CH_4 was calculated in this range for the pertinent experimental conditions (temperature, pressure, and cell length) using line parameters from the HITRAN database [50] (see Sec. III A below for a detailed description of the model). Next, the inverse fast Fourier transform (iFFT) of this model spectrum was fit linearly to the iFFT of the measured spectrum with an amplitude factor as the only fitting parameter. A step weighing function was applied to both the model and the data (after iFFT) to remove the first 1000 points from the fit, where the baseline contribution is strongest. Afterwards, a residual of the fit was calculated over all data points, and a step weighting function was applied to keep the first 1000 points of the residual and zero pad all other points. The weighted residual transformed back to the frequency domain yielded a smoothed baseline with a resolution of 0.3 cm^{-1} (9 GHz) interpolated to the resolution of the measurement (250 MHz). This baseline was used to normalize the transmission spectra. The same procedure was repeated for the 125 individual spectra recorded with different f_{rep} values. The normalized spectra were interleaved to yield the final spectrum with 2-MHz sampling point spacing. The relative noise on the baseline in the middle of the spectrum averaged 16 times was 4×10^{-4}, which corresponds to a noise equivalent absorption coefficient of 7.2×10^{-6} cm^{-1} after 3.2 h averaging.

III. DATA TREATMENT AND FITTING

A. Doppler-broadened lines

The entire probe spectrum spans 5900–6100 cm^{-1} and an example of a spectrum recorded with the pump locked to the $R(0)$ line in the ν_3 fundamental band with perpendicular relative pump-probe polarization is shown in Fig. 3 in Companion Paper [36]. The central part of this spectrum, i.e., lines $P(4)$ through $R(4)$, is shown in black in Fig. 4 below. The relative intensities and the Doppler widths of these lines carry information about the sample temperature. Therefore, to estimate the sample temperature we fit a multiline model to the central part of the Doppler-broadened $2\nu_3$ overtone spectrum shown in Fig. 4 (the weak lines between the R branch transitions belong to other bands of CH_4 and do not influence the result of the fit because of their low signal-to-noise ratio). In the model, the partition function and the frequencies, lower state energies, and intensities of the transitions were taken from the HITRAN database [50]. The line shape of each transition was assumed to be Gaussian. The optical path length was fixed to 55 cm (corresponding to the cooled part of the cell) and the pressure was fixed to the experimental value listed in Table I. The temperature dependence of the line intensities was modeled using Eq. (A11) in Ref. [55], and temperature was the only fitting parameter. The orange (gray) curve in Fig. 4 shows the result of the fit, which returned a temperature of 110.92(3) K. Because of the temperature gradients in the cell, the Doppler-broadened response is not purely Gaussian, as shown by the zoom on the $R(0)$ line in the inset (note that the sub-Doppler V-type transition does not affect the fit). However, the fit is more sensitive to the relative intensities of the lines, and it clearly indicates that the temperature is higher than 77 K. A similar fit to a Doppler-broadened spectrum recorded with the pump off yielded a temperature of 101.0(1) K. We attribute the fact that the temperature is higher than 77 K to inefficient cooling by liquid nitrogen and the temperature gradient at the edges of the Dewar. The fits to the Doppler-broadened spectra taken with the pump locked to the nine different transitions returned a temperature of 111(4) K, where the uncertainty is the standard deviation for all data sets. The increase of the temperature with the pump on is in good agreement with numerical simulations of radial heat transport, which yield a 7-K temperature increase for the pump locked to the $R(0)$ line.

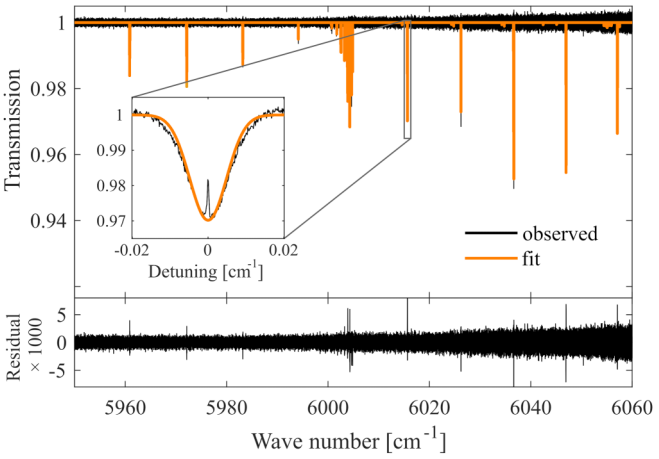

FIG. 4. Part of the Doppler-broadened spectrum (black) measured at 30 mTorr with pump locked to the $R(0)$ fundamental transition and perpendicular relative pump-probe polarizations (same as shown in Fig. 3 in Companion Paper [36]) together with a fit of a model [orange (gray)] used to extract the temperature of the sample. The residuum is shown in the lower panel.

B. Sub-Doppler lines

The V-type probe transitions can be easily found in the spectrum as they appear in the centers of the

Doppler-broadened lines sharing the lower level with the pump transition. However, the positions of the ladder-type probe transitions are not known *a priori*, therefore we implemented a numerical procedure to identify them in the spectrum. The interleaved spectrum was first divided by a model of the Doppler-broadened $2\nu_3$ overtone spectrum, based on the HITRAN parameters [50] and the pertinent experimental conditions (same as described in Sec. III A, but calculated over the entire probe range of 5900–6100 cm^{-1}), to remove the contribution from the Doppler-broadened response from the spectrum. Next, to enhance the narrow sub-Doppler peaks, the spectrum was convolved with a 20-MHz-wide (HWHM) Lorentzian dispersive function to reduce the influence of noise and the residuum of the Doppler-broadened lines. Thereafter, the first derivative of the spectrum was calculated. Since the noise level across the spectrum was varying, the spectrum was normalized by a moving mean of the square of the spectrum calculated over a window of 10 000 points (i.e., 20 GHz, or 0.667 cm^{-1}). Finally, a peak finding routine (MATLAB "findpeaks" function) was applied with a threshold set to detect peaks with a signal-to-noise ratio (SNR) above unity. To reject false detections (some peaks with SNR close to 1), all detected peaks were inspected visually.

To retrieve the center frequency, the width, and the peak value of each double-resonance probe transition, a Lorentzian function was fit to the unmodified interleaved spectrum. The fitting range was $\pm 0.004\,\mathrm{cm}^{-1}$ (± 120 MHz) around each transition. First, the central part of this range ($\pm 0.001\,\mathrm{cm}^{-1}$, ± 30 MHz) was masked and a second order polynomial was fit to the baseline and subtracted from the data to remove the Doppler-broadened background caused by elastic collisions. After that, the Lorentzian function was fit with center frequency, width and amplitude as fitting parameters using a custom-written implementation of the Levenberg-Marquardt algorithm. The uncertainties (standard errors) of the fit parameters were calculated as the square root of the diagonal covariance matrix elements. The quality factor of each fit was calculated as the ratio of the fit amplitude and the rms of the residual.

As an example, the data and the fits to the probe transitions detected with the pump locked to the $P(3, F_2)$ transition in the ν_3 fundamental band are shown in Fig. 5 for the V-type [panels (a)–(c)] and the ladder-type excitations [panels (d)–(f)] using perpendicular (black) and parallel [orange (gray)] relative pump-probe polarizations. The V-type transitions are shown together with the Doppler-broadened background of the corresponding line from the $2\nu_3$ band (in the fitting range of $\pm 0.004\,\mathrm{cm}^{-1}$). Since the different symmetry components of the $P(3)$, $Q(3)$, and $R(3)$ Doppler-broadened lines overlap, the sub-Doppler V-type transitions appear on sloping backgrounds. The assignment of the ladder-type probe transitions shown in Figs. 5(d)–5(f) is based on TheoReTS (see Sec. IV A below). Figure 5 in Companion Paper [36] shows three additional examples of ladder-type transitions detected with the pump locked to the $R(0)$ transition in the ν_3 fundamental band, together with fits and residua. The results of the fits to all lines are summarized in Tables II and III in Sec. IV.

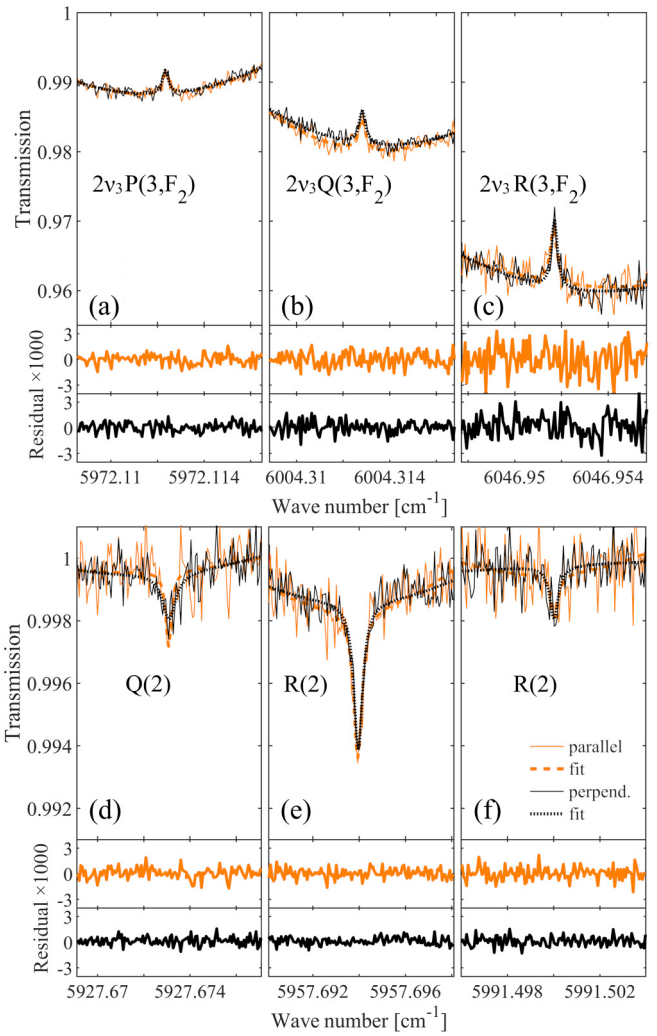

FIG. 5. The (a)–(c) V-type and (d)–(f) ladder-type double-resonance probe transitions detected with the pump laser locked to the $P(3, F_2)$ fundamental transition for parallel [orange (gray)] and perpendicular (black) relative pump-probe polarizations. The thin curves in the upper panels show the data, while the thick curves display the fits of the Lorentzian model and a second order polynomial baseline [dashed orange (gray) for parallel polarization and dotted black for perpendicular polarization]. The x-scale range in all panels is 0.008 cm^{-1}. Note the different y-scale ranges for the V-type and ladder-type probe transitions. The two lower panels show the corresponding residuals of the fits.

IV. LINE PARAMETERS

A. Center frequencies and widths

The wave numbers of the double-resonance probe transitions were calculated as a weighted mean of the wave numbers found from the fits to the probe transitions measured using parallel and perpendicular relative pump-probe polarizations. The inverse of the square of the fit uncertainty (i.e., the variance) was used as a weight. The weight was put to zero for all lines for which the quality factor was less than 2 [e.g., the orange (gray) curve in Fig. 5(a) or the black curve in Fig. 5(b) in Companion Paper [36]]. The standard deviation of

TABLE II. Experimental wave numbers (column 3) and widths (column 4) of the V-type probe transitions (column 2), corresponding to transition frequencies in the $2\nu_3$ overtone band, detected with pump laser locked to different pump transitions in the ν_3 fundamental band (column 1).

Pump transition ν_3 band	Probe transition $2\nu_3$ band	Probe transition wave number (cm^{-1})	Probe transition HWHM (MHz)
$R(0)$	$R(0)$	6015.66382(4)	6.2(2)
$R(1)$	$R(1)$	6026.22685(5)	5.6(3)
	$Q(1)$	6004.86265(5)	5.6(4)
	$P(1)$	5994.14368(5)	7(1)
$Q(1)$	$R(1)$	6026.22684(5)	4.9(4)
	$Q(1)$	6004.86264(5)	4.4(4)
	$P(1)$	5994.14370(5)	4(1)
$P(1)$	$R(1)$	6026.22687(5)	4.6(3)
	$Q(1)$	6004.86265(5)	4.7(4)
	$P(1)$	5994.14371(5)	7(1)
$P(2, E)$	$R(2,E)$	6036.65385(5)	6(1)
	$P(2, E)$	5983.18341(5)	6(1)
$P(2, F_2)$	$R(2, F_2)$	6036.65764(5)	4.2(4)
	$Q(2, F_2)$	6004.64356(5)	6.2(6)
	$P(2, F_2)$	5983.19366(5)	3.9(5)
$P(3, A_2)$	$R(3, A_2)$	6046.96358(5)	3.9(4)
	$Q(3, A_2)$	6004.29224(5)	3.7(4)
	$P(3, A_2)$	5972.13391(5)	3.9(5)
$P(3, F_1)$	$R(3, F_1)$	6046.94204(5)	2.7(3)
	$Q(3, F_1)$	6004.32864(5)	4.4(6)
	$P(3, F_1)$	5972.09529(5)	4.3(7)
$P(3, F_2)$	$R(3, F_2)$	6046.95168(5)	4.5(5)
	$Q(3, F_2)$	6004.31281(5)	5.2(5)
	$P(3, F_2)$	5972.11235(5)	4.7(5)

the weighted mean was calculated using the assumption that the inverse of the variance of the weighted mean is equal to the sum of the inverse of the variances of the two values. This standard deviation was below $3\times10^{-5}\,cm^{-1}$ for all V-type lines and for most of the ladder-type lines. The uncertainty originating from the drift of the pump center frequency (1.33 MHz, or $4.3\times10^{-5}\,cm^{-1}$; see Sec. II A above) was added in quadrature to the standard deviation to yield the total uncertainty.

The wave numbers of the V-type probe transitions are summarized in column 3 of Table II. Column 1 indicates the pump transition in the ν_3 fundamental band while column 2 denotes the probe transition in the $2\nu_3$ overtone band. The frequency of the $Q(2,E)$ probe transition with pump on the $P(2, E)$ line is not reported because of the too low SNR. In Companion Paper [36] we compared the frequencies of the $R(0)$, $R(1)$, $Q(1)$, $Q(3, A_2)$ and $P(3, A_2)$ probe transitions to data available from previous high-accuracy measurements of the $2\nu_3$ band [22,24] and found agreement to within 0.5 MHz, confirming the high accuracy of our measurements.

The last column of Table II reports the HWHM of the probe transitions, weighted in the same way as the transition wave numbers. These widths are in the 3–7-MHz range, dominated by the power broadening by the pump.

The results for the ladder-type probe transitions are summarized in Table III. Column 1 indicates the pump transitions in the ν_3 fundamental band and their upper state term values (corresponding to the lower state term values of the probe transitions) taken from Refs. [19,20]. Column 2 shows the ΔJ assignments of the probe transitions based on the TheoReTS database (see below). Column 3 states the experimental probe transition wave numbers, while column 4 gives the corresponding final state term values, calculated as the sum of the lower energy level of the probe transition (column 1) and the experimental probe transition frequency (column 3). Column 7 lists the HWHM of the probe transitions, which are all in the 6–10-MHz range. The fact that the ladder-type probe transitions are wider than the V-type probe transitions is a consequence of the convolution over the molecular velocities (Doppler shifts) [37]. For co-propagating pump and probe, the linewidths of the V- and ladder-type transitions are three and five times the homogeneous broadening calculated from the power broadening, respectively.

Column 5 shows the term values of the final states reached in the optical-optical double-resonance measurements of de Martino *et al.* [33–35]. The resolution of that experiment was three orders of magnitude lower than in our measurement, and not sufficient to resolve the splittings in pump and probe spectra for initial $J > 1$. For these cases, the previously measured transitions should be viewed as blends of more than one transition, the final states of which are now resolved in our

TABLE III. Summary of the results for the ladder-type probe transitions detected for different pump transitions, listed in column 1. The experimental transition wave numbers and final state term values are listed in columns 3 and 4, respectively. Column 5 contains the final state term values from the work of de Martino *et al.* [33–35] and column 6 the differences δ between the term values from our work and those references. Column 7 lists the HWHM of the probe transitions. Columns 8–11 show the predicted transition wave numbers, the difference with respect to our observed wave numbers, Einstein A coefficients, and final state assignments from TheoReTS (upper number) and ExoMol (lower numbers, in italics) databases (for details, see text). The probe transition assignments in column 2 are from TheoReTS.

1 Pump transition in the ν_3 band and its upper state term value (cm^{-1})	2 Probe transition	3 Probe transition wave number (cm^{-1})	4 Final state term value (cm^{-1})	5 Final state term value from Refs. [33–35] (cm^{-1})	6 δ our work and Refs. [33–35] (cm^{-1})	7 Probe transition width (MHz)	8 Transition wave number (cm^{-1}) TheoReTS *ExoMol*	9 Obs-Calc (cm^{-1}) TheoReTS *ExoMol*	10 Einstein A coefficient (s^{-1}) TheoReTS *ExoMol*	11 Final state assignment TheoReTS *ExoMol*
$R(0)$ 3028.752260	$R(1)$	6046.36008(5)	9075.11234(5)			7(1)	6046.36012	-0.00004	0.3065	$3\nu_3(F_2)$43%
							6041.50853	*4.85*	*0.265*	$2\nu_4(2)+2\nu_3(2,1)$
	$P(1)$	5979.16720(5)	9007.91946(5)			10(1)	5979.27374	-0.11	0.5291	$2\nu_2+2\nu_3(A_1)$20%; $\nu_1+4\nu_2(A_1)$17%
							5988.43179	*-9.26*	*0.0893*	$\nu_1+4\nu_2(0)$
	$P(1)$	5946.58753(5)	8975.33979(5)	8975.34	-0.00021	7.4(1.0)	5947.15944	-0.57	0.6881	$\nu_1+4\nu_2(A_1)$37%; $3\nu_3(A_1)$19%
							5944.79368	*1.79*	*1.06*	$3\nu_3(3,0)$
	$Q(1)$	5929.25825(5)	8958.01051(5)	8957.96	0.05051	10.0(8)	5928.37576	0.88	1.523	$3\nu_3(F_1)$52%; $\nu_1+3\nu_3(F_1)$14%
							5921.95684	*7.28*	*1.40*	$3\nu_3(3,3)$
	$R(1)$	5910.8068(1)	8939.5591(1)	8939.56	-0.0009	10(3)	5910.30937	0.50	0.1907	$3\nu_3(F_2)$22%
							5911.91331	*-1.11*	*0.0545*	$3\nu_3(1,1)$
$R(1)$ 3048.980142	$R(2)$	6056.48376(5)	9105.46390(5)			5(1)	6056.48569	-0.0019	0.2971	$3\nu_3(F_2)$63%
							6059.95092	*-3.47*	*0.2100*	$2\nu_2(2)+\nu_3(2,2)$
	$P(2)$	5969.66090(6)	9018.64104(6)			6(1)	5969.81250	-0.15	0.2601	$2\nu_2+2\nu_3(A_1)$20%; $\nu_1+4\nu_2(A_1)$18%
							5957.02649	*12.63*	*0.0138*	$\nu_1+4\nu_2(4)$
	$P(2)$	5937.7677(1)	‡ 8986.7478(1)	8986.75	-0.0022	12(4)	5938.38891	-0.62	0.3313	$\nu_1+4\nu_2(A_1)$35%; $3\nu_3(A_1)$18%
							5941.62828	-3.86	*0.5686*	$5\nu_2(1)+\nu_4(1,1)$
	$Q(2)$	5929.28494(5)	* ** 8978.26508(5)	8978.25	0.01503	9.4(6)	5928.42915	0.86	1.131	$3\nu_3(F_1)$49%
							5922.91515	6.27	*1.030*	$3\nu_3(3,3)$
	$R(2)$	5922.67986(6)	8971.66000(6)	8971.67	-0.0100	8(2)	5922.41619	0.26	0.1574	$3\nu_3(F_2)$4.5%; $\nu_1+2\nu_2+\nu_3(F_2)$4.3%
							5922.15254	0.53	*0.0400*	$3\nu_3(3,1)$
	$P(2)$	5909.24115(9)	† 8958.22129(9)	8958.21	0.01129	10(3)	5908.39180	0.85	0.5623	$\nu_1+3\nu_3(F_1)$66%
							5911.77247	2.53	*0.5630*	$\nu_1+2\nu_2(2)$
$Q(1)$ 3029.306115	$R(1)$	6046.06828(6)	9075.37440(6)			3(2)	6046.06790	0.00038	0.2395	$3\nu_3(F_2)$50%
							6047.31528	-1.25	*0.166*	$2\nu_2(0)+2\nu_3(2,2)$
	$Q(1)$	5957.44166(5)	‡ 8986.74778(5)	8986.75	-0.00222	7(1)	5958.05332	-0.61	0.2536	$\nu_1+4\nu_2(A_1)$35%; $3\nu_3(A_1)$18%
							5954.51826	*5.92*	*0.4191*	$3\nu_3(3,1)$
	$R(1)$	5948.95899(5)	* ** 8978.26511(5)	8978.25	0.01511	8.2(7)	5948.09357	0.87	0.3814	$3\nu_3(F_1)$52%
							5941.90699	*7.05*	*0.350*	$3\nu_3(3,3)$
	$Q(1)$	5928.91510(5)	† 8958.22122(5)	8958.21	0.01122	9.5(1.0)	5928.05621	0.86	0.411	$3\nu_3(F_1)$51%; $\nu_1+3\nu_3(F_1)$14%
							5921.49626	*7.42*	*0.329*	$3\nu_3(3,3)$
	$P(1)$	5918.93759(5)	8948.24371(5)	8948.24	0.00371	8.5(9)	5918.04234	0.9	1.524	$3\nu_3(F_1)$52%; $\nu_1+3\nu_3(F_1)$14%
							5911.36914	*7.57*	*1.369*	$3\nu_3(3,3)$

TABLE III. (*Continued.*)

1 Pump transition in the ν_3 band and its upper state term value (cm^{-1})	2 Probe transition	3 Probe transition wave number (cm^{-1})	4 Final state term value (cm^{-1})	5 Final state term value from Refs. [33–35] (cm^{-1})	6 δ our work and Refs. [33–35] (cm^{-1})	7 Probe transition width (MHz)	8 Transition wave number (cm^{-1}) TheoReTS *ExoMol*	9 Obs-Calc (cm^{-1}) TheoReTS *ExoMol*	10 Einstein A coefficient (s^{-1}) TheoReTS *ExoMol*	11 Final state assignment TheoReTS *ExoMol*
$P(1)$ 3019.493054	$R(0)$	6035.94676(5)	9055.43981(5)			7.0(9)	6035.94784	-0.0011	0.1885	$3\nu_3(F_2)45\%$
							6037.37538	*-1.43*	*0.148*	$3\nu_3(3,1)$
	$R(0)$	5938.72822(5)	† 8958.22127(5)	8958.21	0.01127	8.3(4)	5937.86487	0.86	0.5272	$3\nu_3(F_1)51\%; \nu_1+3\nu_3(F_1)14\%$
							5931.29424	*7.43*	*0.450*	$3\nu_3(3,1)$
$P(2,E)$ 3030.502542	$Q(1)$	6025.12811(6)	9055.63065(6)			8(1)	6025.12942	-0.0013	0.4052	$3\nu_3(F_2)46\%$
							6026.28916	*-1.16*	*0.0714*	$3\nu_3(3,1)$
	$R(1)$	5978.87023(6)	9009.37277(6)	9009.45*	-0.07723	8(2)	5979.53197	-0.66	0.1852	$\nu_1+4\nu_2(A_1)30\%; 3\nu_3(A_1)17\%$
							5982.03201	*-3.16*	*0.289*	$5\nu_2(1)+\nu_4(1,1)$
	$R(1)$	5948.19655(5)	8978.69909(5)	8978.68*	0.01909	7.1(5)	5947.44947	0.75	0.7171	$3\nu_3(F_1)35\%$
							5942.21200	5.98	*0.4532*	$5\nu_2(5)+\nu_4(1,1)$
$P(2,F_2)$ 3030.436420	$R(1)$	6009.74667(5)	9040.18309(5)			7(1)	6009.96960	-0.22	0.1166	$2\nu_2+2\nu_3(A_1)19\%; \nu_1+4\nu_2(A_1)19\%$
							6010.19063	*-0.44*	*0.0504*	$2\nu_2(2)+2\nu_3(2,1)$
	$R(1)$	5979.04297(5)	9009.47939(5)	9009.45*	0.02930	8(1)	5979.71487	-0.67	0.1841	$\nu_1+4\nu_2(A_1)30\%; 3\nu_3(A_1)17\%$
							5976.4276	*2.62*	*0.284*	$5\nu_2(3)+\nu_4(1,1)$
	$R(1)$	5948.26760(5)	8978.70402(5)	8978.68*	0.02402	8.0(5)	5947.67461	0.59	0.5842	$3\nu_3(F_1)52\%$
							5942.0546	*6.21*	*0.2742*	$3\nu_3(3,3)$
	$Q(1)$	5928.30687(6)	8958.74329(6)			9(2)	5927.41421	0.89	0.3772	$3\nu_3(F_1)65\%$
							5930.22954	*-1.92*	*0.1408*	$2\nu_2(2)+2\nu_3(2,0)$
$P(3,A_2)$ 3051.673466	$R(2)$	6054.50217(6)	9106.17564(6)			7(2)	6054.50220	-0.00003	0.2095	$3\nu_3(F_2)46\%$
							6062.53717	*-8.04*	*0.1173*	$7\nu_4(7,4)$
	$P(2)$	6006.10212(6)	9057.77559(6)			6(1)	6006.10160	0.00052	0.5225	$3\nu_3(F_2)47\%$
							6006.4862	*-0.38*	*0.0165*	$3\nu_3(3,1)$
	$R(2)$	5992.03737(5)	9043.71084(5)			6.3(1.0)	5992.78685	-0.75	0.2275	$\nu_1+4\nu_2(A_1)24\%; 3\nu_3(A_1)16\%$
							5985.69361	*6.34*	*0.2484*	$3\nu_3(3,0)$
	$R(2)$	5957.70612(5)	9009.37959(5)	9009.45*	-0.07041	6.7(4)	5957.29062	0.42	0.7031	$3\nu_3(F_1)35\%; \nu_1+3\nu_3(F_1)9\%$
							5951.46747	*6.24*	*0.4149*	$5\nu_2(3)+\nu_4(1,1)$
	$Q(2)$	5927.864(2)	8979.538(2)	8979.52*	0.018	7(5)	5926.98221	0.88	0.4877	$3\nu_3(F_1)52\%; \nu_1+3\nu_3(F_1)14\%$
							5929.54232	*-1.68*	*0.4068*	$5\nu_2(5)+\nu_4(1,1)$
$P(3,F_1)$ 3051.909263	$R(2)$	5991.06680(6)	9042.97593(6)			7(1)	5991.78249	-0.72	0.2289	$\nu_1+4\nu_2(A_1)25\%; 3\nu_3(A_1)16\%$
							5983.50119	*7.57*	*0.3648*	$\nu_3(3,0)$
	$R(2)$	5957.67296(5)	9009.58209(5)	9009.45*	0.13209	6.4(4)	5957.33600	0.34	0.6526	$3\nu_3(F_1)24\%; 2\nu_2+2\nu_3(A_1)8.5\%$
							5949.52695	*8.15*	*0.4992*	$3\nu_3(3,3)$
	$Q(2)$	5927.52678(5)	8979.43591(5)	8979.52*	-0.08409	8(1)	5926.66173	0.87	0.5201	$3\nu_3(F_1)52\%$
							5919.92487	*7.60*	*0.4466*	$3\nu_3(3,3)$
$P(3,F_2)$ 3051.809388	$R(2)$	5991.50002(6)	9043.30941(6)			7(2)	5992.23818	-0.74	0.2277	$\nu_1+4\nu_2(A_1)25\%; 3\nu_3(A_1)16\%$
							5983.7642	*7.74*	*0.2167*	$3\nu_3(3,0)$
	$R(2)$	5957.69395(5)	9009.50334(5)	9009.45*	0.05334	6.8(5)	5957.35843	0.34	0.6498	$3\nu_3(F_1)31\%$
							5949.71501	*7.98*	*0.4915*	$3\nu_3(3,3)$
	$Q(2)$	5927.67308(5)	8979.48247(5)	8979.52*	-0.03753	6.7(1.0)	5926.80471	0.87	0.5044	$3\nu_3(F_1)52\%$
							5920.66232	*7.01*	*0.1671*	$3\nu_3(3,3)$

work. Therefore we list the final states from Refs. [33–35] for each of our observed transitions that contributes to one of theirs. We marked with an asterisk (*) those cases when more than one of our states contribute to a term value determined previously. Column 6 shows the difference between the final state term values from the two measurements, which are all below 0.13 cm^{-1}. We note that in three cases the same final state is reached in our work by different combinations of transitions [e.g., $P(1)$-$R(0)$ and $Q(1)$-$Q(1)$]. These states are marked by symbols ‡, $^{*}_{**}$, and † in column 4. The term values agree within their uncertainties, which again confirms the high precision of our measurement.

The following columns show comparisons of the ladder-type transition parameters to theoretical prediction from the TheoReTS [39] (upper number) and ExoMol [41] (lower number, in italics) databases. Column 8 shows the transition wave numbers, column 9 the difference between the observed and the predicted transition wave numbers, and column 10 the Einstein A coefficients of the transitions. The last column lists the assignments of the final states.

The TheoReTS database provides a list of high temperature transitions containing the center wave numbers, the line intensities at the requested temperature (up to 2000 K), the lower energy levels, and the self- and air-broadening coefficients (the two last parameters are constant for all lines). The Einstein A coefficients, as well as the two main vibrational mode contributions and their amplitude factors (see below), were provided on request. The predicted TheoReTS transitions were identified by searching the database for transitions with a lower state energy corresponding to the upper level of the pump transitions within a ± 0.05 cm^{-1} window. When the lower levels listed in TheoReTS were not equal to the HITRAN energy levels [50], the energy difference $E_{\mathrm{HITRAN}} - E_{\mathrm{TheoReTS}}$ was subtracted from the TheoReTS transition wave numbers to correct for this discrepancy. This procedure allowed identifying between three and ten TheoReTS lines for each pump transition within the measured probe spectral range. The strongest lines matched the detected probe transitions to within 1 cm^{-1}. We note that the frequency difference between predicted lines sharing the lower level is a few tens of cm^{-1}, allowing unambiguous assignment. The difference between the observed and the predicted transition wave numbers is listed in column 9 and plotted in Fig. 4 in Companion Paper [36]. The mean difference is 0.19 cm^{-1} and the mean of the absolute values of the difference is 0.52 cm^{-1}. The assignment of the measured transitions shown in column 2 was deduced from the upper and lower J values of the corresponding predicted transitions.

The ExoMol database contains a file that lists state numbers, term values, and a complete set of quantum number assignments for over one million calculated eigenvalues, sorted by the J value (up to 12), then symmetry, and then the term value (up to 23 000 cm^{-1}). The assignments are based upon the largest base set contribution to each eigenstate. Another series of files gives all calculated transitions grouped in 100-cm^{-1} intervals, ordered by the transition wave numbers, with the Einstein A coefficients and the lower and upper state numbers. Most of the transitions are highly forbidden, so the dynamic range of the Einstein A coefficients is large. For example, in the range between 5900 and 6100 cm^{-1}, 136 transitions from the upper level of the $P(3, F_1)$ pump transition are tabulated with Einstein A coefficients spanning the range 5×10^{-1}–1×10^{-8} s^{-1}. Examination of the predicted transitions in the region of the ν_3 fundamental band provided unambiguous assignment of the state label numbers for the upper states of the pump transitions. However, unlike the case of the TheoReTS list, assignments of the observed ladder-type probe transitions to specific lines in the ExoMol list are not always unambiguous. In each case, we selected the transition starting from the assigned pumped state to a state with the same J value as predicted by TheoReTS that had a large Einstein A coefficient and was nearest to the observed transition wave number. These ExoMol transition wave numbers are listed in column 8 of Table III, in each case in italics and below the values from the TheoReTS list. Similarly, the difference between the observed and the predicted ExoMol wave numbers is listed in column 9, and the predicted Einstein A coefficients are listed in column 10. The mean difference is 3.08 cm^{-1} and the mean absolute value of the difference is 5.05 cm^{-1}. It is evident that the predictions of the ExoMol list are about an order of magnitude less precise than those of the more recent TheoReTS list in this energy region.

The final state assignments from TheoReTS and ExoMol lists are given in column 11. In the 6000-cm^{-1} range the strongest transitions from the ground state are to the $2\nu_3(F_2)$ state. This suggests that the $3\nu_3 \leftarrow \nu_3$ transitions should be the strongest in the double-resonance spectrum. The $3\nu_3$ states are near the top of the $n = 6$ polyad and are expected to be least affected by Fermi resonances with the states with two quanta in the bending modes (ν_2, ν_4). Despite this, it is evident from the assignments predicted by theory, presented in Table III, that there is substantial state mixing in this region. In the $3\nu_3$ states, vibrational substates with symmetries $A_1 + F_1 + 2F_2$ are infrared active from the F_2 symmetry $\nu_3 = 1$ state [56], all four of which are expected to contribute to the spectra. A complete description of a normal mode state includes total vibrational quantum number for each mode (n_1, n_2, n_3, n_4), a vibrational angular momentum quantum number (l_2, l_3, l_4) for degenerate vibrational normal modes, and an angular momentum projection quantum number (m_3, m_4) for the two triply degenerate normal modes [57]. The ExoMol database lists all these quantum numbers for the dominant contribution to each state as $n_1\nu_1 + n_2\nu_2(l_2) + n_3\nu_3(l_3, m_3) + n_4\nu_4(l_4, m_4)$. Those numbers are listed in italics in column 11. The TheoReTS database provided only the total vibrational quantum numbers and vibrational symmetries for the largest two contributions to each eigenfunction. These are listed above the ExoMol assignment. The percent values are 100 times the square of the amplitude for the listed basis state. For some transitions, the basis functions with the largest contribution have the same labels. In these cases, we added the contributions from these states. It needs to be pointed out that assignment solely based on the largest one or two contributions to the wave function expansion can be misleading, especially when eigenstates are highly delocalized over the basis functions used in the variational calculation.

B. Line intensities

To evaluate the accuracy of theoretical predictions of hot methane spectra, not only the wave-number accuracy of individual lines must be estimated but also the relative accuracy of

individual transition intensities. Accurate absolute experimental line intensities of ladder-type probe transitions are difficult to obtain from the double-resonance measurements because the exact population in the lower levels of the probe transitions is not known. However, assuming equal collision relaxation rates for the upper and lower states of the pump transition, the steady state population in the pumped state should match the depletion of the ground state, which can be estimated from the fractional absorption dip in the V-type transitions. Therefore, we normalize the areas of the ladder-type probe transitions to the area of the V-type probe transition in the Doppler-broadened line corresponding to the pump transition, which removes the dependence on the population of the intermediate state. We then compare these normalized intensities to predictions based on the parameters from the HITRAN and TheoReTS databases.

The area of each measured double-resonance probe transition was calculated as the product of the fit peak value and width (HWHM) multiplied by π. Next, the weighted means of the areas measured with parallel and perpendicular relative pump-probe polarizations were calculated, where the weight was 1 for parallel polarization and 2 for perpendicular, which yields an isotropic average independent of the value of the M quantum number. The experimental normalized intensities $\bar{I}_{\mathrm{E}}$ were calculated by dividing the weighted area of each ladder-type probe transition by the weighted area of the corresponding V-type probe transition. When the pump was locked to transitions with $J_{\mathrm{low}} > 0$ and multiple V-type transitions were detected, we chose for normalization the area of the V-type probe transition with the same J_{up} as the pump transition. For example, with the pump on the ν_3 $P(3, F_2)$ transition, we chose the V-type transition in the $2\nu_3$ $P(3, F_2)$ transition, shown in Fig. 5(a). This gives the same relative weight for different M values of the two transitions, because linear absorption transitions with the same initial and final J values have the same M dependence of the cross sections.

The predicted normalized intensities were calculated as $\bar{I}_{\mathrm{P}} = (A^{\mathrm{pro}} g_j^{\mathrm{pro}} / A^{\mathrm{pum}} g_j^{\mathrm{pum}})(v_{ij}^{\mathrm{pum}} / v_{ij}^{\mathrm{pro}})^2$, where A^k is the spontaneous emission rate (the Einstein A coefficient) of the transition, g_j^k is the upper state degeneracy, and v_{ij}^k is the transition wave number for the probe and pump transitions, where k stands for probe (pro) or pump (pum). HITRAN parameters were used for the $2\nu_3$ band transitions (i.e., the V-type probe transitions) and the TheoReTS line list was used for the ladder-type probe transitions.

Figure 6 shows the logarithms (base 10) of the experimental (red circular markers, $\log_{10}\bar{I}_{\mathrm{E}}$) and predicted (black square markers, $\log_{10}\bar{I}_P$) normalized intensities. The different panels correspond to different pump transitions, as marked in the panel. In general, the agreement is reasonably good and further supports the assignments. In particular, the relative intensities of the different probe transitions in the individual panels are reproduced well. The agreement between the measured and predicted normalized intensities is particularly good for the $Q(1)$, $P(2, E)$, and $P(3, F_2)$ pumping cases. To illustrate that, Table IV lists, in column 2, the mean and standard deviation of the relative discrepancies between the logarithms of the experimental and predicted normalized intensities, $\log_{10}(\bar{I}_{\mathrm{E}}/\bar{I}_P)$, for each pump transition. Column 3 shows the same values expressed as linear ratios, i.e., as $\bar{I}_{\mathrm{E}}/\bar{I}_P$.

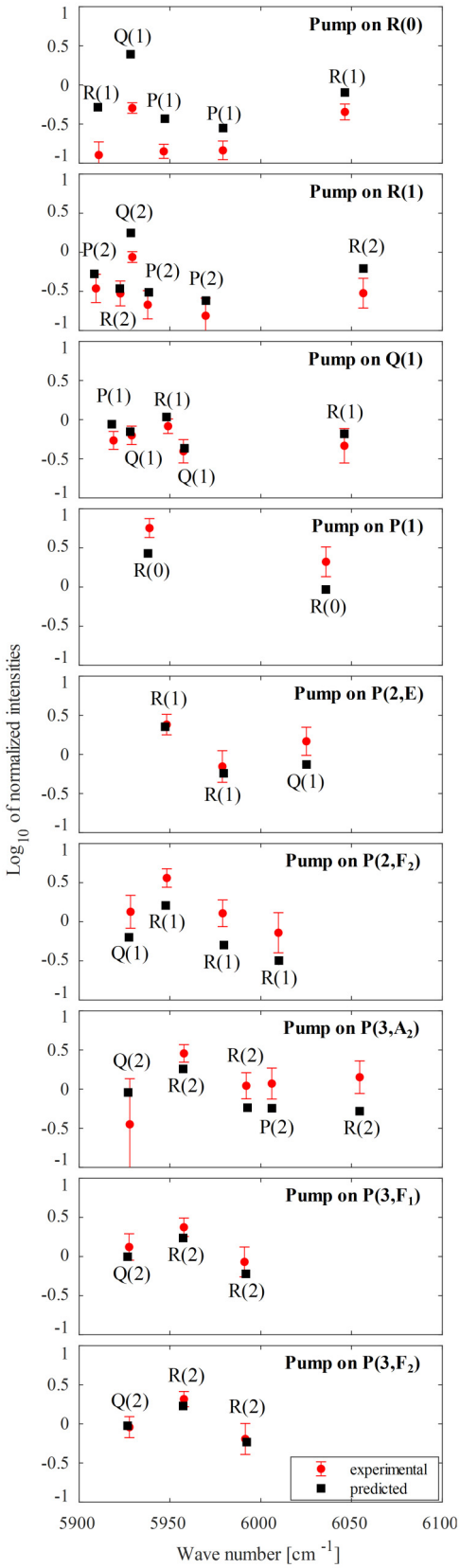

FIG. 6. Logarithm (base 10) of the experimental (red circular markers) and predicted (black square markers) normalized intensities. See text for details.

TABLE IV. Column 2 shows the mean (and standard deviation, in parentheses) of the logarithms (base 10) of the ratios of the experimental ($\bar{I}_E$) and predicted ($\bar{I}_P$) normalized intensities shown in Fig. 6. Column 3 shows the mean (and standard deviation) of the linear ratios between the experimental and predicted normalized intensities.

Pump transition ν_3 band	Mean of $\log_{10}(\bar{I}_E/\bar{I}_P)$	Mean of $\bar{I}_E/\bar{I}_P$
$R(0)$	−0.45(19)	0.38(16)
$R(1)$	−0.204(95)	0.64(14)
$Q(1)$	−0.112(71)	0.78(13)
$P(1)$	−0.340(21)	2.2(1)
$P(2, E)$	0.14(14)	1.4(5)
$P(2, F_2)$	0.360(33)	2.30(18)
$P(3, A_2)$	0.16(33)	1.7(9)
$P(3, F_1)$	0.138(15)	1.37(5)
$P(3, F_2)$	0.036(53)	1.09(13)

Significant deviations from 0 (or 1 for the linear ratios) beyond the experimental uncertainties are evident for the $R(0)$, $R(1)$, $P(1)$, $P(2, F_2)$, and $P(3, A_2)$, $P(3, F_1)$ pumping cases. These results can be used to estimate the relative precision of the predicted intensities.

V. CONCLUSIONS

We report here on the detection and assignment of 36 sub-Doppler resolution double-resonance transitions in methane reaching 32 final states in the $3\nu_3$ band region. The measurement was done using a high-power cw pump and a comb probe, whose spectrum was detected using a mechanical Fourier transform spectrometer with comb-mode-limited resolution. The transition center frequency accuracy was in the 1.3-3 MHz range, limited by the pump frequency stability. This allowed determination of the final state term values with three orders of magnitude better accuracy than the previous optical-optical double-resonance measurements [33–35].

The parameters of the transitions were compared to theoretical predictions from the TheoReTS and ExoMol databases. The agreement between the center frequencies is an order of magnitude better with TheoReTS than with ExoMol, and thus the TheoReTS line list was used for line assignment. The assignment was confirmed by the normalized transition intensities (i.e., the ratio of the areas of the ladder-type probe transitions and their corresponding V-type probe transitions).

Future work aims at detection of a larger number of double-resonance transitions to highly excited levels of methane with better frequency and intensity accuracy. To achieve higher absorption sensitivity, we will replace the single pass cell with an enhancement cavity for the comb. To increase the pump stability, we will lock the pump laser directly to the comb. These improvements will allow detection of a wide range of weaker probe transitions with high signal to noise ratio.

ACKNOWLEDGMENTS

The authors thank Michael Rey for providing additional information from the TheoReTS database, Hiroyuki Sasada for providing the ground state upper state term values, and Jin Guo and Chuang Lu for help with setting up the cw-OPO. A. Foltynowicz acknowledges the Swedish Research Council (Grant No. 2016-03593) and the Knut and Alice Wallenberg Foundation (Grant No. KAW 2015.0159). G.S. acknowledges the Foundation for Polish Science (Grant No. POIR.04.04.00-00-434D/17-00). O.A. acknowledges the Swedish Research Council (Grant No. 2015-04374) and the Kempe Foundations (Grant No. JCK 1317.1).

[1] A. R. W. McKellar, Can. J. Phys. **67**, 1027 (1989).
[2] S. N. Yurchenko, J. Tennyson, J. Bailey, M. D. J. Hollis, and G. Tinetti, Proc. Natl. Acad. Sci. USA **111**, 9379 (2014).
[3] M. A. K. Khalil, M. J. Shearer, and R. A. Rasmussen, Methane sinks distribution, in *Atmospheric Methane: Sources, Sinks, and Role in Global Change* (Springer, Berlin, Heidelberg, 1993), pp. 168–179.
[4] S. M. Henrichs and W. S. Reeburgh, Geomicrobiol. J. **5**, 191 (1987).
[5] M. Hirtzig, B. Bézard, E. Lellouch, A. Coustenis, C. de Bergh, P. Drossart, A. Campargue, V. Boudon, V. Tyuterev, P. Rannou *et al.*, Icarus **226**, 470 (2013).
[6] M. R. Swain, G. Vasisht, and G. Tinetti, Nature (London) **452**, 329 (2008).
[7] M. R. Swain *et al.*, Astrophys. J. **704**, 1616 (2009).
[8] M. R. Swain *et al.*, Nature (London) **463**, 637 (2010).
[9] G. Guilluy, A. Sozzetti, M. Brogi, A. S. Bonomo, P. Giacobbe, R. Claudi, and S. Benatti, Astron. Astrophys. **625**, A107 (2019).
[10] R. J. Tancin, Z. Chang, M. Gu, V. Radhakrishna, R. P. Lucht, and C. S. Goldenstein, Opt. Lett. **45**, 583 (2020).
[11] M. Rey, A. V. Nikitin, and V. G. Tyuterev, Astrophys. J. **847**, 105 (2017).
[12] R. J. Hargreaves, I. E. Gordon, M. Rey, A. V. Nikitin, V. G. Tyuterev, R. V. Kochanov, and L. S. Rothman, Astrophys. J. Suppl. Ser. **247**, 55 (2020).
[13] A. Wong, P. F. Bernath, M. Rey, A. V. Nikitin, and V. G. Tyuterev, Astrophys. J. Suppl. Ser. **240**, 4 (2019).
[14] M. Ghysels, S. Vasilchenko, D. Mondelain, S. Beguier, S. Kassi, and A. Campargue, J. Quant. Spectrosc. Radiat. Transfer **215**, 59 (2018).
[15] R. Georges, J. Thievin, A. Benidar, S. Caries, B. Amyay, M. Louviot, V. Boudon, and J. Vander Auwera, Rev. Sci. Instrum. **90**, 093103 (2019).
[16] O. N. Ulenikov, E. S. Bekhtereva, S. Albert, S. Bauerecker, H. M. Niederer, and M. Quack, J. Chem. Phys. **141**, 234302 (2014).
[17] R. L. Barger and J. L. Hall, Phys. Rev. Lett. **22**, 4 (1969).
[18] S. N. Bagaev and V. P. Chebotaev, JETP Lett. **16**, 433 (1972).
[19] S. Okubo, H. Nakayama, K. Iwakuni, H. Inaba, and H. Sasada, Opt. Express **19**, 23878 (2011).

[20] M. Abe, K. Iwakuni, S. Okubo, and H. Sasada, J. Opt. Soc. Am. B **30**, 1027 (2013).
[21] P. A. Kocheril, C. R. Markus, A. M. Esposito, A. W. Schrader, T. S. Dieter, and B. J. McCall, J. Quant. Spectrosc. Radiat. Transfer **215**, 9 (2018).
[22] C. Ishibashi, M. Kourogi, K. Imai, B. Widiyatmoko, A. Onae, and H. Sasada, Opt. Commun. **161**, 223 (1999).
[23] C. Ishibashi and H. Sasada, Jpn J. Appl. Phys., Part 1 **38**, 920 (1999).
[24] A. M. Zolot, F. R. Giorgetta, E. Baumann, W. C. Swann, I. Coddington, and N. R. Newbury, J. Quant. Spectrosc. Radiat. Transfer **118**, 26 (2013).
[25] A. V. Nikitin, V. Boudon, C. Wenger, S. Albert, L. R. Brown, S. Bauerecker, and M. Quack, Phys. Chem. Chem. Phys. **15**, 10071 (2013).
[26] A. V. Nikitin, O. M. Lyulin, S. N. Mikhailenko, V. I. Perevalov, N. N. Filippov, I. M. Grigoriev, I. Morino, Y. Yoshida, and T. Matsunaga, J. Quant. Spectrosc. Radiat. Transfer **154**, 63 (2015).
[27] V. M. Devi *et al.*, J. Mol. Spectrosc. **315**, 114 (2015).
[28] V. M. Devi *et al.*, J. Quant. Spectrosc. Radiat. Transfer **177**, 152 (2016).
[29] A. Campargue, O. Leshchishina, L. Wang, D. Mondelain, and S. Kassi, J. Mol. Spectrosc. **291**, 16 (2013).
[30] A. V. Nikitin, I. S. Chizhmakova, M. Rey, S. A. Tashkun, S. Kassi, D. Mondelain, A. Campargue, and V. G. Tyuterev, J. Quant. Spectrosc. Radiat. Transfer **203**, 341 (2017).
[31] M. Ghysels, D. Mondelain, S. Kassi, A. V. Nikitin, M. Rey, and A. Campargue, J. Quant. Spectrosc. Radiat. Transfer **213**, 169 (2018).
[32] A. V. Nikitin, A. E. Protasevich, M. Rey, V. I. Serdyukov, L. N. Sinitsa, A. Lugovskoy, and V. I. G. Tyuterev, J. Quant. Spectrosc. Radiat. Transfer **239**, 106646 (2019).
[33] A. de Martino, R. Frey, and F. Pradere, Chem. Phys. Lett. **111**, 113 (1984).
[34] A. de Martino, R. Frey, and F. Pradere, Mol. Phys. **55**, 731 (1985).
[35] M. de Chevalier and A. de Martino, Chem. Phys. Lett. **135**, 446 (1987).
[36] A. Foltynowicz, L. Rutkowski, I. Silander, A. C. Johansson, V. Silva de Oliveira, O. Axner, G. Soboń, T. Martynkien, P. Mergo, and K. K. Lehmann, Phys. Rev. Lett. **126**, 063001 (2021).
[37] M. S. Feld and A. Javan, Phys. Rev. **177**, 540 (1969).
[38] V. S. Petrovic and R. W. Field, J. Chem. Phys. **128**, 014301 (2008).
[39] M. Rey, A. V. Nikitin, Y. L. Babikov, and V. G. Tyuterev, J. Mol. Spectrosc. **327**, 138 (2016).
[40] S. N. Yurchenko and J. Tennyson, Mon. Not. R. Astron. Soc. **440**, 1649 (2014).
[41] J. Tennyson *et al.*, J. Mol. Spectrosc. **327**, 73 (2016).
[42] I. Silander, T. Hausmaninger, W. G. Ma, F. J. M. Harren, and O. Axner, Opt. Lett. **40**, 439 (2015).
[43] O. Axner, W. G. Ma, and A. Foltynowicz, J. Opt. Soc. Am. B **25**, 1166 (2008).
[44] G. C. Bjorklund, Opt. Lett. **5**, 15 (1980).
[45] G. C. Bjorklund, M. D. Levenson, W. Lenth, and C. Ortiz, Appl. Phys. B **32**, 145 (1983).
[46] A. Foltynowicz, Ph.D. thesis, Umeå University, 2009.
[47] T. Hausmaninger, I. Silander, and O. Axner, Opt. Express **23**, 33641 (2015).
[48] G. Sobon, T. Martynkien, D. Tomaszewska, K. Tarnowski, P. Mergo, and J. Sotor, Photon. Res. **6**, 368 (2018).
[49] P. F. Bernath, *Spectra of Atoms and Molecules*, 4th ed. (Oxford University Press, New York, 2020).
[50] I. E. Gordon *et al.*, J. Quant. Spectrosc. Radiat. Transfer **203**, 3 (2017).
[51] A. Foltynowicz, T. Ban, P. Maslowski, F. Adler, and J. Ye, Phys. Rev. Lett. **107**, 233002 (2011).
[52] P. Maslowski, K. F. Lee, A. C. Johansson, A. Khodabakhsh, G. Kowzan, L. Rutkowski, A. A. Mills, C. Mohr, J. Jiang, M. E. Fermann, and A. Foltynowicz, Phys. Rev. A **93**, 021802(R) (2016).
[53] L. Rutkowski, P. Maslowski, A. C. Johansson, A. Khodabakhsh, and A. Foltynowicz, J. Quant. Spectrosc. Radiat. Transfer **204**, 63 (2018).
[54] R. K. Cole, A. S. Makowiecki, N. Hoghooghi, and G. B. Rieker, Opt. Express **27**, 37920 (2019).
[55] L. S. Rothman *et al.*, J. Quant. Spectrosc. Radiat. Transfer **60**, 665 (1998).
[56] M. S. Child and L. Halonen, Adv. Chem. Phys. **57**, 1 (1984).
[57] D. Papousek and M. R. Aliev, *Molecular Vibrational and Rotational Spectra* (Elsevier, Amsterdam, 1982), Vol. 17.